Mapping subsea permafrost around Tuktoyaktuk Island (NWT, Canada) using electrical resistivity tomography

Ephraim Erkens[1,2], Michael Angelopoulos[1], Jens Tronicke[2], Scott R. Dallimore[3], Dustin Whalen[4], Julia Boike[1,5], and Pier Paul Overduin[1]

[1]Alfred Wegener Institute, Helmholtz Centre for Polar and Marine Research, Potsdam, Germany
[2]University of Potsdam, Institute of Geosciences, Potsdam, Germany
[3]Geological Survey of Canada, Sidney, British Columbia, Canada
[4]Natural Resources Canada, Geological Survey of Canada – Atlantic, Dartmouth, Nova Scotia, Canada
[5]Humboldt University, Geography Department, Berlin, Germany

Correspondence: Ephraim Erkens (ephraimerkens@gmail.com)

Abstract. Along much of the Arctic coast, shoreline retreat and sea level rise combine to inundate permafrost. Once inundated by seawater permafrost usually begins to degrade. Tuktoyaktuk Island (Beaufort Sea, NWT, Canada) is an important natural barrier protecting the harbor of Tuktoyaktuk, but will likely be breached within the next three decades. The state of subsea permafrost and its depth distribution around the island are, however, still largely unknown. We collected marine electrical re-

5 sistivity tomography (ERT) surveys (vertical electrical soundings) north and south of Tuktoyaktuk Island using a floating cable with 13 electrodes in a quasi-symmetric Wenner-Schlumberger array. We filtered the data with a new approach to eliminate potentially falsified measurements due to a curved cable and inverted the profiles with a variety of parameterizations to estimate the position of the top of the ice-bearing permafrost table (IBPT) below the sea floor. Our results indicate that north of Tuktoyaktuk Island, where coastal erosion is considerably faster, IBPT depths range from 5 m below sea level (120 m from

10 the shoreline) to around 20 m bsl (up to 800 m from the shoreline). South of the island, the IBPT dips more steeply and lies at 10 m bsl a few meters from the shore to more than 30 m bsl 200 m from the shore. We discuss how marine ERT measurements can be improved by recording electrode position, but choices made in data inversion can be a more likely source of uncertainty in IBPT position than electrode positions. At Tuktoyaktuk Island, IBPT depths below the sea floor increase with distance from the shoreline; comparing the northern and southern sides of the island, its inclination is inversely proportional to coastline

15 retreat rates. On the island's north side, historical coastal retreat rate suggests a mean degradation rate of 5.3 ± 4.0 cm/yr.

1 Introduction

Coastal erosion and retreat have severe infrastructure and socioeconomic consequences in the Arctic (Irrgang et al., 2019; Ramage et al., 2021). It also transforms permafrost from terrestrial to subsea, which may amplify erosion as it degrades in a positive feedback (Solomon et al., 2008). In addition, the potential release of greenhouse gases from thawing permafrost

20 might contribute to global warming as a positive feedback mechanism (Schuur et al., 2015) but despite the large subsea carbon stocks the amount emitted to the atmosphere is still debated (Miesner et al., 2023). This study examines the use of a geo-

physical method to estimate the current degradation rate of subsea permafrost at Tuktoyaktuk Island (Beaufort Sea, Northwest Territories, Canada) and discusses potential sources of uncertainty that may arise from the survey design and technologies employed.

25   Subsea permafrost (the terms *offshore*, *submarine* or *subaquatic* can be used synonymously) is predominantly relic terrestrial permafrost, formed during the Last Glacial Maximum (LGM) or earlier and inundated during marine transgression (Kitover et al., 2016). Locally, subsea permafrost can also form in shallow waters, when the water column freezes completely during winter (*bottom-fast ice* or *bedfast ice*), resulting in sub-zero benthic temperatures and freezing of the seabed sediment (Solomon et al., 2008). Since the LGM, sea level has risen by approximately 120 m, resulting in an estimated subsea permafrost area of

30    $2.5 \cdot 10^6$ km^2 (Overduin et al., 2019).

After inundation, subsea permafrost naturally warms. Thawing can happen from below due to the geothermal gradient (*bottom-up thawing*) or from the top downwards if the bottom seawater temperatures are higher than the freezing point of the permafrost (*top-down thawing*). In marine environments, salt diffusion into the sediment porewater lowers the freezing point which causes the thawing of permafrost below Arctic waters with a negative mean annual temperature (Angelopoulos et al.,

35   2019). The lowering of the top of the permafrost (0 °C isotherm or top of ice-bearing permafrost table; IBPT) is referred to as permafrost degradation. Although this is a natural process, anthropogenic climate change and increasing air and water temperatures, especially in Arctic regions where atmospheric temperatures in some localities are rising 4 times faster than the global mean (Rantanen et al., 2022), may strongly accelerate subsea permafrost degradation (Wilkenskjeld et al., 2022).

Tuktoyaktuk Island is affected by rapid coastal erosion and is projected to be breached within the next 20 years which will

40   have important socio-economic consequences for the hamlet of Tuktoyaktuk. The study of subsea permafrost around the island is important to understand the effects of coastal erosion and can support the planning of coastline protection measures. Subsea permafrost thaw may lead to enhanced coastal erosion as seafloor subsidence potentially allows more powerful waves which accelerate erosion of the bluff (Dallimore et al., 1996). To mitigate coastal erosion and to prolong the sheltering effect of the island so that the community has more time to adapt, coastal protection measures are planned. Knowledge of the permafrost

45   depth distribution around the island will provide useful information to build effective protection structures.

Marine electrical resistivity tomography (ERT) has been used to detect subsea permafrost (Angelopoulos, 2022). The method relies on the high resistivity contrast between frozen fresh water saturated and unfrozen salt water saturated sediment and uses a floating electrode cable dragged by a boat for current injection and voltage measurements (Fig. 2). As opposed to terrestrial ERT surveys where electrode positions are fixed, a flexible cable in a marine ERT survey relies on potentially varying electrode

50   positions. Previous studies have accounted for deviating electrode positions only by visually assessing the cable straightness from the boat during the measurements (cf. Overduin et al., 2012, 2016; Angelopoulos et al., 2019).

The objective of this study is to better understand how coastal retreat and subsea permafrost thawing have shaped subsea permafrost around Tuktoyaktuk Island based on marine ERT surveys and to provide a more constrained estimation of IBPT depth distribution over a spatially more extended area north and south of the island.
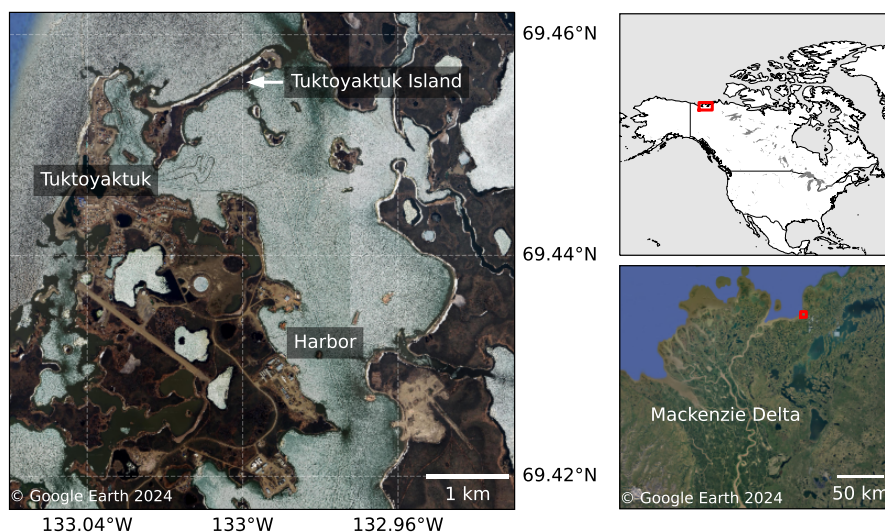
Figure 1. Overview map of the research area. Tuktoyaktuk Island is located close to the hamlet of Tuktoyaktuk, east of the Mackenzie Delta in Northwestern Canada. The barrier island protects the harbor from incoming storms and waves.

2 Methods

2.1 Study region

Tuktoyaktuk Island is a barrier island in the Beaufort Sea (NWT, Canada), next to the hamlet of Tuktoyaktuk (Fig. 1). The island is an important protection for the hamlet and its harbor as it shelters both from wind and waves. The northwestern shore is exposed to the ocean and characterized by a beach of 1 to 6 m width, followed by a ca. 4 to 6 m high cliff. Sediments making up the island consist of Quaternary-aged, ice bonded sands and silt with some random massive ice bodies which are deformed indicating glacial overriding (Lapham et al., 2020). On top of the cliff, the island is mostly flat and covered by lowland and highland tundra with active layer depths around 60 cm. The permafrost thickness in the area is estimated at 400 m (Hu et al., 2013).

Since the onset of Arctic amplification in 1970, air temperatures in the region are rising twice as fast as the global average (Hansen et al., 2010; Lenssen et al., 2019): 0.052 °C per year on average in the past 50 years to a current mean annual temperature of -8 °C (Lenssen et al., 2019; Lapham et al., 2020; GRID-Arendal, 2020). Rising temperatures lead to an extension of the open water period, which accelerates coastal retreat due to thermoerosion (Berry et al., 2021). The coastal retreat rate at the island and the area of Tuktoyaktuk has been recorded since 1947 by the GSC using aerial photography, remote sensing and ground based GPS surveys (Hynes et al., 2014). The northwestern coastline retreats particularly rapidly, at rates that have risen from 1.58 ± 0.05 m/yr to 1.80 ± 0.02 m/yr in the past 20 years (Whalen et al., 2022). The southeastern coastline retreats much slower but rates have also increased in the 21st century to currently 0.48 ± 0.04 m/yr. Considering that the

island measures only 36 m across at the narrowest point and around 50 m over most of its stretch, Whalen et al. (2022) predict that it will be breached at the latest by the year 2044.

75   This will have severe consequences for the harbor of Tuktoyaktuk: it will be exposed to incoming storms as the most significant storms are from the north and northwest (Manson and Solomon, 2007; Kokelj et al., 2012). The harbor is of traditional and economic importance to the community and to shipping, providing a basis for transportation and supply for other communities in the Inuvialuit Settlement Region, as well as an operating base for the Canadian Coast Guard Service. Numerous shore protection measures have been used to mitigate coastal erosion along the shore face of the community starting in the 1970s, such as concrete blocks to fill up space left by thaw subsidence, or geotextile to protect the sediment from mobilization via the

80 incoming waves, but all have been damaged within a couple of years (Baird, 2019a). Currently, armourstone is still in place at several locations along the coast but does not prevent coastal retreat. A more recent study suggests mitigation of coastal erosion at the hamlet and Tuktoyaktuk Island with sand reservoirs (Baird, 2019b).

2.2   Study design

In September 2021, we collected more than 30 marine ERT profiles around Tuktoyaktuk Island, orientated roughly parallel

85 or perpendicular to the shoreline. Each profile consisted of numerous (tens to several hundred, depending on the length of the profile) adjacent vertical electrical soundings (VES) in a quasi-symmetric reciprocal Wenner-Schlumberger array. We used a floating multicore cable towed behind a boat to collect the soundings at a spacing of around 5 m. The cable offered 22 outputs of which we used 13 (2 injection electrodes and 11 potential electrodes) resulting in 10 roughly vertically stacked soundings with a quasi-common center but different effective depths of investigation (Fig. 2). Current was injected at the center of the

90 cable with 10 m separation between the injection electrodes. The potential electrode pairs outside of the injection electrodes were separated by 15 m to 115 m. The positions of electrode pairs at intermediate separations were slightly changed between the two days of acquisition. The measurements were recorded with an *IRIS Syscal Pro Deep Marine™* as a control unit, together with the *IRIS* software *Sysmar™* on a connected field laptop. The water depth was measured from the boat for every sounding using an echosounder. GPS positions at the boat and at the center and tail of the cable were continuously recorded.

95 In addition, water conductivity and temperature profiles were measured next to and in between some of the ERT profiles using either a *Sontek Castaway™* or an *AML Oceanography™* CTD.

    Assessment of the terrestrial and nearshore geology and of the nearshore bathymetry benefited by previous studies led by the Geological Survey of Canada (Boike and Dallimore, 2019) and completion of two terrestrial boreholes on Tuktoyaktuk Island and two nearshore boreholes was conducted in 2018 (Lapham et al., 2020).

100 ## 2.3   Analysis

The goal of the data analysis was to invert the ERT data to get a set of intersecting 2D resistivity models that could be used to determine the depth to the top of the permafrost (i.e. the IBPT). We used the permafrost depth in combination with historical coastline data to estimate the resulting vertical permafrost degradation rate.
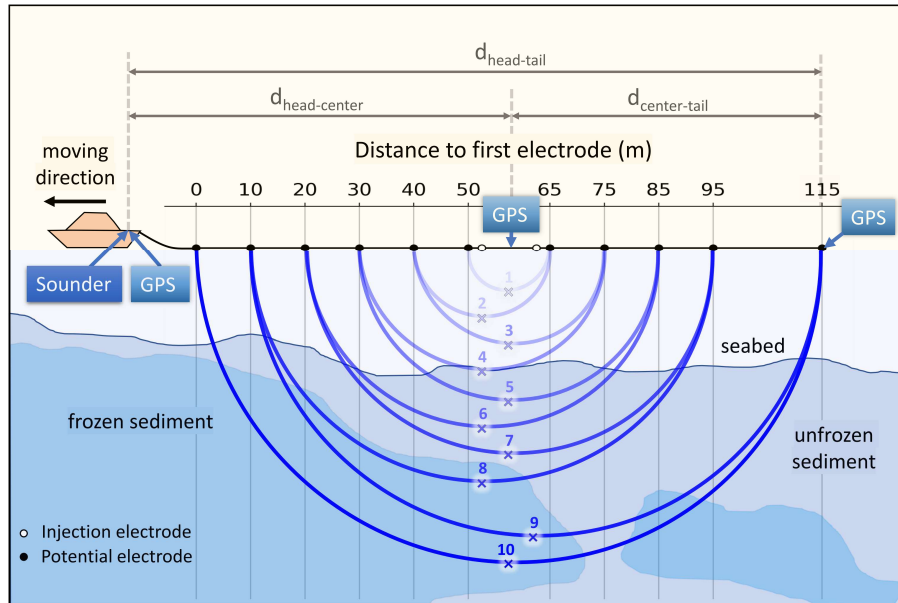
Figure 2. Marine ERT survey setup with floating electrodes. The potential electrode pairs have a quasi-common center but different pseudo-depths (depth of highest sensitivity, marked as 'x'), thus forming VES. GPS units were mounted on the boat (head), between the injection electrodes (center) and at the last potential electrode (tail) respectively to assess the cable curvature based on the distances between the GPS units.

Before inverting the data, soundings with falsified apparent resistivities needed to be removed. In a mobile marine survey
105   electrode positions can potentially vary as the cable is flexible. A curved cable can lead to a change in the geometric factor and thus falsified apparent resistivities as they are linearly dependent. Therefore, we quantified the curvature of the cable during the field measurements using the GPS data from the boat ('head') and the center and tail of the cable. For a straight cable, the sum of the two segments 'head-center' and 'center-tail' is equal to the length 'head-tail'. The difference between those distances $d_d = d_{head-center} + d_{center-tail} - d_{head-tail}$ increases with increasing curvature. Under the most simple assumption of a
110   circular bend, electrode positions along the curved cable could be determined for different values of d_d (Fig. 3a). Based on the modified electrode positions, the modified geometric factor k was calculated for every potential electrode pair (cf. Loke, 2001). Considering the deviation of k for different degrees of curvature as well as the actual GPS data from the field, we derived a curvature (d_d) threshold above which measurements should be regarded as falsified. Those soundings were excluded from the dataset. Where the exclusion led to data gaps in the profiles, the profiles were truncated into individual sections.
115   Every section in the filtered dataset was then inverted in 1D with lateral constraints (LCI) using *Aarhus Workbench™* to construct 2D resistivity models (cf. Auken et al., 2005). Aarhus Workbench offers four inversion types: smooth, blocky, sharp and layered. The different inversion types have different penalizing parameters regarding the minimization of the vertical resistivity contrast between cells and thus result in models with different degrees of sharpness. The inversion can be refined for each inversion type by varying lateral and vertical resistivity constraints i.e. by defining a maximum standard deviation of

Table 1. Default constraints for the different inversion types available in Aarhus Workbench. The vertical constraints should always be looser than the lateral constraints for the representation of a layered medium. The discretization implies that the layered model has no vertical resistivity constraints and that the other three models have no lateral thickness constraints.

Constraints		Inversion type			
		Smooth	Blocky	Sharp	Layered
Lateral resistivity constraints	Loose	1.6	1.6	1.1	1.6
	Medium	1.3	1.3	1.04	1.3
	Tight	1.1	1.1	1.02	1.1
Vertical resistivity constraints	Loose	4	4	1.24	-
	Medium	2	2	1.12	-
	Tight	1.5	1.5	1.06	-
Lateral thickness constraints	Loose	-	-	-	1.6
	Medium	-	-	-	1.3
	Tight	-	-	-	1.1

120   the resistivity contrasts between neighboring cells (Table 1). We followed the recommendations in the manual by varying the lateral and vertical resistivity constraints between the default values for loose, medium and tight constraints.

To provide a basis for comparison of the results from the four inversion types, we tested combinations of inversion types and constraints on an synthetic model to determine the most suited inversion technique for the specific setting. The synthetic model was set up in pyGIMLi (Rücker et al., 2017) and based on information on the local permafrost conditions from two

125   technical reports that contain exemplary permafrost depths below the seabed and electrical resistivities of the terrestrial permafrost (Dallimore et al., 2018; Baird, 2020). The synthetic model consisted of 3 layers representing the water column, the unfrozen sediment and the frozen sediment respectively. Resistivities were constant throughout the layers at 6.1 Ωm, 10 Ωm and 1000 Ωm. The water layer had a depth of around 5 m and the interface between the second and third layer was slightly dipping at varying angles. Through a forward operation following the survey design used in the field, ERT data was simulated

130   that subsequently could be inverted in Aarhus Workbench.

In addition to testing four inversion types, we tested three approaches to determine the interface between unfrozen and frozen sediment (i.e. the IBPT depth): (1) a fixed resistivity range in which the transition from unfrozen to frozen is assumed to occur following previous studies (Fortier et al., 1994; Overduin et al., 2012, 2016), (2) the highest vertical resistivity gradient in linear space and (3) the highest vertical resistivity gradient in logarithmic space. Those criteria were applied to the resistivity models

135   obtained from the inversion of the simulated data. The combination of inversion type, constraints and IBPT determination approach that resulted in the smallest offset between the estimated IBPT and the synthetic model IBPT was assessed to provide the most accurate estimated IBPT depth and therefore applied to the entire dataset. We distinguished between the following terms:

– *estimated IBPT*: depth of highest vertical resistivity contrast in the inversion result (in linear or logarithmic space)

140   – *synthetic model IBPT*: fixed boundary between the second and third layer in our synthetic model, representing the IBPT.

To quantify the offset, we used the RMS of the difference along each column of the inversion grid aiming to put a stronger weight on columns with a greater offset between the estimated IBPT and the synthetic model IBPT.

We used historical coastline data to estimate the time since inundation along our profiles. The coastlines were digitized from 19 aerial photographs taken between 1947 and 2001 and combined with more recent GPS measurements and satellite imagery.

145   The data were first presented by (Solomon, 2005) and later GIS compiled by (Hynes et al., 2014). Since the vast majority of our profile lines lie outside of the 1947 coastline, we extrapolated the time since inundation linearly to every sounding coordinate (with a mean coastal retreat rate of 2 m/yr). Along with the permafrost depth from our ERT surveys we used the time since inundation to estimated the average vertical permafrost degradation rate through linear regression.

3   Results

150   ### 3.1   Geometry

3.1.1   Geometric factor variation

The first source of uncertainty arising from a curved cable is the deviation of the geometric factor from that of a straight cable, because the relative distances between the electrodes change. It appears that for a perfectly circular bent cable, the relative change of the geometric factor $k/k_{straight}$ is proportional to the distance difference d_d (Fig. 3b). The rate of change increases

155   with electrode spacing, i.e. the inner electrodes pairs deviate less than the outer electrode pairs. The deviation for a circular bend remains relatively small for all electrode pairs. Even for relatively high degrees of curvature (corresponding to $d_d = 3$ m) k is only increased by 7 ‰ for the outermost electrode pair. For an irregularly bent cable, the ratios of the distances between electrodes can be expected to change to a greater degree and have a larger effect on the geometric factor. For example, the geometric factor variation is larger if the cable is only partly curved, as the electrode positions are no longer symmetrical

160   and the ratios between the distances considered in the calculation of the geometric factor are disturbed. Although simulations showed that it is possible to have only a slight or even no variation of k with an asymmetrically bent cable (for very specific configurations) the deviation is most often larger. It is therefore not possible to choose a universal threshold for the deviation of k below which the soundings can be considered acceptable and to filter the data accordingly to the corresponding distance difference. Instead, a distance difference threshold must be set iteratively and by considering the second source of uncertainty

165   as well.

3.1.2   Lateral deviation

The second source of uncertainty in a mobile marine survey is the lateral deviation of the cable center from the GPS-recorded boat path (Fig. 3). The sensitivity of the electrode array is predominantly concentrated below the injection electrodes at the
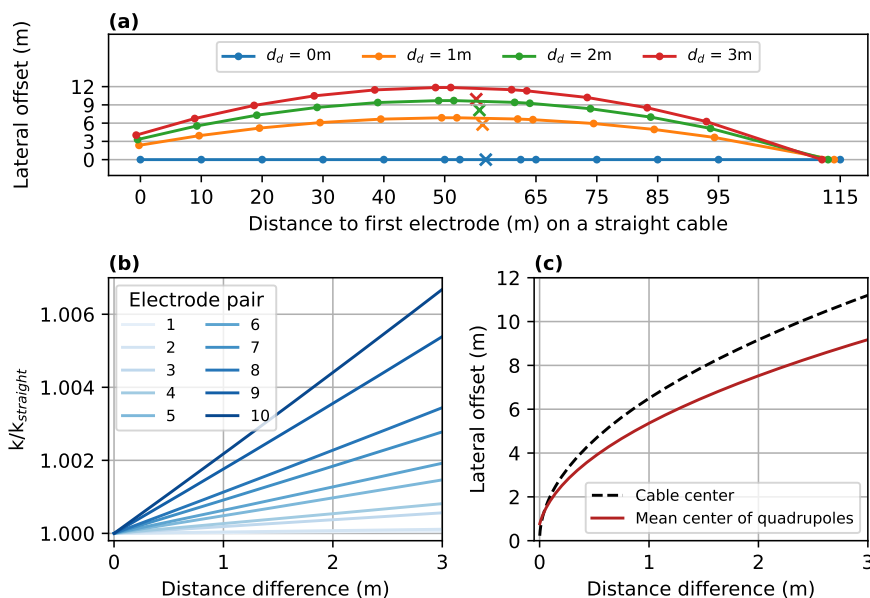
Figure 3. Sources of uncertainty arising from a curved cable. **(a)** Top view of curved cable configurations. The dots represent the electrode positions along the cable for different degrees of curvature and the crosses mark the corresponding highest sensitivity area for a VES (i.e. the mean center of the 10 quadrupoles). **(b)** Relative change of the geometric factor depending on the distance difference for the ten potential electrode pairs. **(c)** Lateral offset of the cable center and the mean center of quadrupoles depending on the distance difference.

cable center. Therefore, a survey with a curved cable risks mapping a slightly different sounding location where the boat path
170   deviates from that of the cable center. Especially in areas where the lateral resistivity gradient is high (e.g. when driving parallel
and close to the coastline), wrongly located profiles could have a large effect on the interpreted resistivity model.

     Considering these two theoretical sources of error, we evaluated the performance of different d_d thresholds and found out
that a threshold of 1 m eliminated strongly curved parts of the profiles where both a lateral deviation of the cable center and a
deviation of the true geometric factor were highly probable. Therefore soundings with $d_d > 1$ m were removed from the dataset
175   and not inverted. During part of the acquisition, the center GPS did not record. In this case, we used only the distance from
head to tail as a curvature criterion. We decided to use the soundings during which this distance remained stable, suggesting a
low degree of cable curvature. Soundings for which the difference varied were remove from the dataset.

3.2   Inversion and IBPT depth

We tested smooth, blocky, sharp and layered LCI with varying lateral and vertical resistivity constraints (varying lateral and
180   thickness constraints in the layered inversion; see Table 1) on an synthetic model. Comparing the different approaches to
determine the IBPT from a given inversion as described in subsection 2.3, we found that overall, the IBPT depths calculated
in logarithmic space are up to 10 times closer to the synthetic model IBPT than the ones calculated in linear space. Only in 5

out of 27 of the tested combinations, the IBPT in linear space is (up to 15 %) closer to the synthetic model IBPT. In addition, the IBPT calculated in the linear space lies mostly well below the depth of investigation (DOI; >10 m deeper). In contrast,

185 the IBPT calculated in logarithmic space lies mostly above the DOI and locally only one or maximum two cells below the DOI. The comparison between linear and logarithmic IBPT applies to the smooth, blocky and sharp inversions; in the layered inversions both are the same.

We imposed additional criteria on determinations of the IBPT, mostly to exclude false positives: (1) the IBPT depth had to exceed water depth, as we expect unfrozen sediment on top of the permafrost, (2) the resistivity below the IBPT boundary

190 has to exceed 10 Ωm; a lower resistivity was assumed to correspond to unfrozen sediment (cf. Overduin et al., 2012) and (3) the median gradient for every model had to exceed 0.02 Ωm/m. This last criterion was determined empirically and applied to exclude inversions with only a subtle peak in the resistivity gradient that would not be a reliable indicator for the IBPT.

A blocky inversion with tight lateral and medium vertical constraints and the corresponding IBPT calculated in linear space respecting the criteria described above identified the IBPT in the synthetic model most precisely. The RMS of the offset between

195 the inferred IBPT from the inversion and the actual boundary of the synthetic model for this inversion type was 2.76 m. The estimated IBPT matched the synthetic model IBPT to a precision below one grid cell size; only towards the rim the offset was larger. A blocky inversion with tight lateral and tight vertical constraints and a sharp inversion with tight lateral and medium vertical constraints showed a similar performance (offset RMS of 2.80 and 3.08 m respectively). The layered inversions were neglected in the comparison as they produced lower RMS values but unrealistic resistivity distributions (correlated electrical

200 resistivity and water depth). For all inversion types, the data residual increases with tightening constraints, but is only used as a secondary quality indicator as the noise level of the measurement cannot be determined and was therefore estimated to be 10 % for the calculation of the data residual. If only individual datum points showed an extremely high residual they were removed before re-running the inversion. This reduced the effect of the outliers on the inversion result and lowered the data residual.

Figure 4 shows the tomogram for a profile perpendicular to the northern shore of Tuktoyaktuk Island (inversion RMS

205 = 11%). The IBPT calculated in linear and logarithmic space are compared to the DOI. The grey dots represent the data points of the inversion and show the cell thickness. The water layer has a resistivity of around 6 Ωm as constrained by the CTD measurements. The unfrozen sediment layer has a similar resistivity with slight variations that may be interpreted as compensation for a slight spatial variation in water resistivity. The transition from unfrozen to frozen layer (as identified by the highest logarithmic resistivity gradient) occurs between 10 and 50 Ωm and the permafrost below shows resistivities of 50

210 to several hundreds Ωm. For the model presented in Fig. 4 the depth of the IBPT is shallow (5 to 10 m bsl) at a distance up to 250 m from the shoreline and descends to a stable level around 20 m bsl further offshore (250 to 600 m from the shore).

The blocky inversion with tight lateral and medium vertical constraints was applied to the whole dataset. Inferred permafrost depths are represented in Fig. 5. It appears that the permafrost depth ranges from 5 to 25 m bsl north of the island at water depths from below 5 to over 20 m. The historical coastlines show that the northern shore facing the open ocean is subject to

215 faster coastal erosion than the southern side. The profiles are mostly outside the historical coastlines as the water was to shallow closer to the coast to be reached with the boat. Therefore, the borehole locations have not been crossed with the ERT surveys. South of the island, the IBPT ranges from 10 to 30 m bsl at water depths from 10 to over 35 m. Several profiles have been
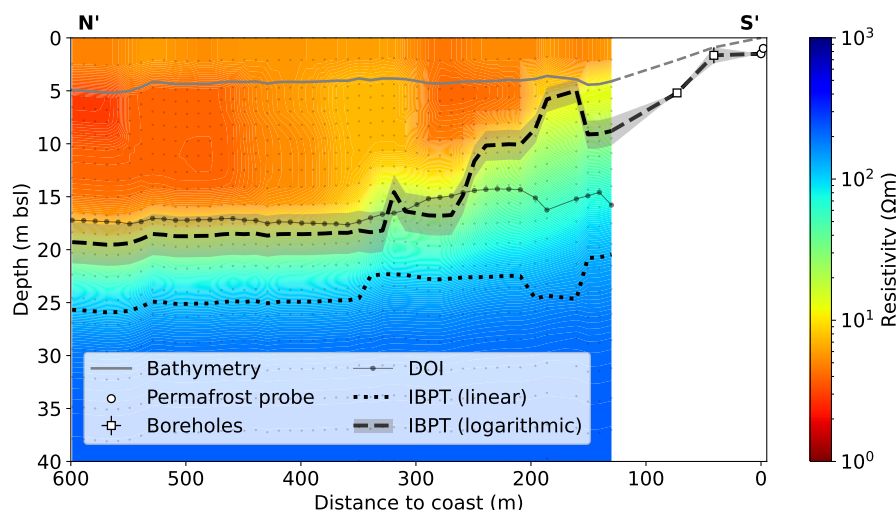
Figure 4. Comparison of IBPT calculations (linear and logarithmic) and DOI in an inverted resistivity model. The model is extended towards the shore based on borehole information (Dallimore et al., 2018) and permafrost probe measurements.

removed south of the island (shaded lines) as they did not return reasonable IBPT depths (i.e. depth well below the DOI, see discussion). Intersections between profiles are thus only found north of the island. They can be used to assess the concordance

220 of our IBPT determination method. Most intersections show a difference in IBPT depth below 10 %, which corresponds to a deviation of 0 or 1 grid cell of the inversion and depending on the depth to an absolute deviation of up to 2 m. However, few intersection show differences in the 15 to 20 % area (2 grid cells or up to 4 m) and one intersection even deviates by 35 %. These percentages are of course dependant on the grid size used in the inversion and the distribution would be more scattered for a finer grid. The raw apparent resistivities at the intersections match very well (average deviation 0.9 ± 1.2 Ωm), which

225 means that the measurement is not dependant on the orientation of the profiles. Deviations in the IBPT at the intersections are therefore most probably originating from lateral constraints.

The vertical subsea permafrost degradation rate was estimated north of the island under the assumption of constant coastal retreat rate within the past 270 years. The IBPT depth used for the calculation was taken from the representative profile shown in Fig. 4 and the inundation time was extrapolated from historical coastline data. According to a linear regression, the degradation

230 rate is 5.3 ± 4.0 cm/yr.

4 Discussion

4.1 Geometry

Our GPS data showed that the distance difference d_d is a reliable indicator for the degree of cable curvature, especially for slight curvatures. From our geometric considerations it is however not possible to quantify the exact deviation of the geometric
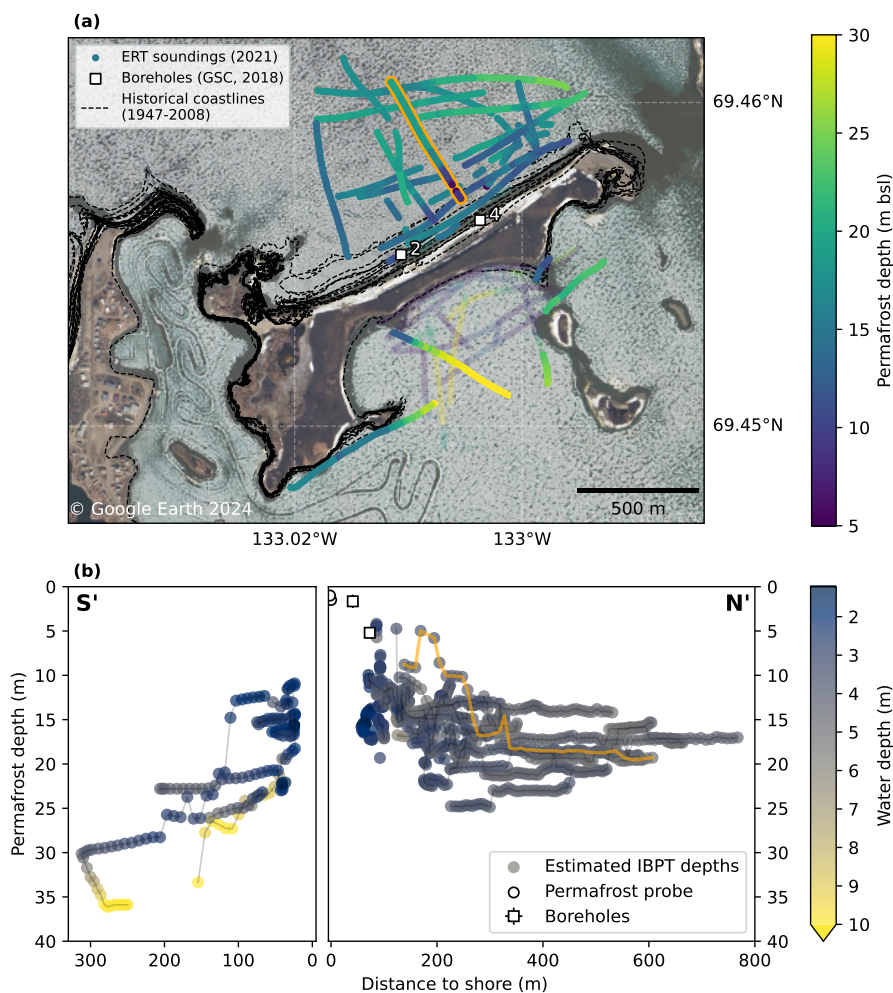
Figure 5. (a) Map view of IBPT depth around Tuktoyaktuk Island. South of the island, several profiles have been removed (transparent lines). The historical coastline since 1947 show the faster degradation of the northern shoreline facing the open ocean (Hynes et al., 2014). Most of the profiles however lie beyond the shoreline of 1947. **(b)** IBPT depth over the distance to the shore, south and north of Tuktoyaktuk Island. The remaining profiles south of the island indicate a steeper slope of the permafrost table compared to the northern side. The profile shown in Fig. 4 is highlighted in orange.

235 factor resulting from the shifted electrode positions because the bent cable may rather have an asymmetric curvature than forming a circular arc. However, even for an asymmetric curvature, soundings with $d_d < 1$ m are only affected negligibly by a deviating geometric factor. To further elaborate the approach of quantifying the cable curvature and the exact deviation of the geometric factor, precise knowledge of all electrode positions would be needed. Given the exact positions, even soundings with a strongly curved cable could be corrected and still used in the further analysis, increasing the amount of available data
240 especially in areas were extended straight boat paths may be unrealistic due the local geography. During a small test campaign, we tested the use of GPS units at every electrode position, but the accuracy of the devices was disturbed and thus not sufficient for exact positioning. Improved GPS accuracy would be desirable in future surveys as exact electrode positioning in marine surveys is very valuable. Other possibilities to reduce the error induced by a curved cable would be to directly control the cable straightness by making use of a second boat at the tail of the cable or by using rigid supporting material along the cable.

245 **4.2 Inversion**

Our inversion showed a relatively high data residual throughout all four inversion types compared to similar studies (e.g. Angelopoulos et al., 2021). However the data residuals are relative values and cannot be used to evaluate the quality of the inversion since the ambient noise level of our measurements is unknown. In order to use the data residual for the comparison and assessment of the different inversion types, repeated measurements (e.g. by anchoring the boat and fixing the cable at the
250 shore or using a second boat) would be needed to estimate the noise level. However the data residual still indicates the relative fit between data points of one model and is often unevenly distributed. This could be explained by slight spacial variations in water salinity or temperature i.e. water resistivity (with salinity being the far dominant factor since temperature changes were only minor). As the water layer forms the large part of the sensitivity area and the layer is constrained in the inversion, it might be difficult to fit the the model to possibly inaccurate water resistivities. Arboleda-Zapata et al. (2022) showed how sensitive
255 the inversion reacts to the water layer resistivity and thus how important it is to constrain the inversion based on a dense net of CTD measurements. In case the water layer is stratified it might even be useful to incorporate two water layers in the inversion, but our CDT measurements indicated a homogeneous water layer.

Although the data residual could not be used to compare the different inversion types and parametrizations, we were able determine a best-suited inversion type for the specific application using a synthetic model. A 3-layer model with constant
260 resistivities is without doubt oversimplified, but is close enough to the real setting to evaluate the performance of the inversion types in the given setting. We are then evaluating if the resistivity distribution obtained in the inversion of the simulated data is reflecting the (synthetic) IBPT by the highest gradient of the logarithmic resistivities. This approach leads to a best-suited inversion type. This evaluation of inversion types is only valid for our specific case, but the approach could potentially be adopted in other studies.

265 We found that the IBPT is best represented using a blocky inversion with tight lateral and medium vertical constraints and by calculating the highest resistivity gradient in logarithmic space. A blocky inversion with tight lateral and tight vertical constraints performs almost equally well, so it was also tested on the field data and returned very similar IBPT depths. The IBPT is often close to the DOI, sometimes slightly below. This can be expected and does not refute our interpretation because

the electric field is expected not to penetrate deep into the permafrost due to its high resistivity, so the DOI is then near the
270   interface from unfrozen to frozen ground. This also implies that the actual resistivities of the permafrost are not reliable and
must be seen only as a contrast to the overlying lower resistivities. The potential ambiguity of the peak in the resistivity
gradient is also important to consider. Especially in the smooth inversion, there are often multiple peaks along the vertical
resistivity gradient, so that there is no clear indication of the IBPT depth. In the blocky and sharp inversion, this problem
does not occur and the peaks are always unique. Nonetheless, it is important to implement additional criteria to avoid that the
275   water-seabed interface is identified as the IBPT or that permafrost is suspected in areas of low resistivities or that a maximum
gradient is picked although there is no big vertical contrast over the whole depth of the model. We addressed this issue by
setting a minimum depth (i.e. $z_{IBPT} > z_{water}$), a minimum resistivity (10 Ωm) and a minimum resistivity gradient (median of
0.02 Ωm/m over the entire model). The latter serves to avoid finding boundaries in a homogeneous resistivity distribution and
was set empirically. Especially for several profiles south of the island with water depths up to 18 m, the penetration depth of
280   the applied measurement configuration is not sufficient to penetrate the sediment deep enough to identify the IBPT. Therefore
the area above the DOI is homogeneous in resistivity (only water) and the automatically detected IBPT lies well below the DOI
where the inverted model is able to create greater resistivity contrasts without changing the forward operation.

     When discussing uncertainties of the reconstructed depth of the IBPT, not only plausible alternative models are important to
consider but also the uncertainties of the 'best-suited' model itself. Due to the discretization using 30 cells with logarithmically
285   increasing thickness below the seabed, the vertical spatial resolution of each model decreases with depth. The water layer
thickness uncertainty is given by the resolution of the bathymetric measurements, at an estimated standard deviation of 10 cm.
The cell thickness of the first layer below the water layer is 1 m. Features that are smaller than the cell size cannot be resolved by
the inversion. Our permafrost probe measurements at the shore revealed permafrost depths greater than 1 m (which corresponds
to the order of sub-aquatic active layer depths; Osterkamp et al., 1989). At 20 m depth (approximate depth of the IBPT from
290   350 to 550 m offshore), the cell thickness is around 2 m which leads to an even lower resolution at that depth and is also the
reason for small but abrupt step-like changes in IBPT depth within only a few metres in the lateral direction. The uncertainties
in IBPT depth due to inversion resolution thus range from $\pm$ 0.5 m to $\pm$ 1 m (half the layer thickness) and need to be considered
when calculating the vertical permafrost degradation rate.

     But there is the potential to obtain a more precise IBPT depth. Besides a finer grid in the inversion, additional measurements
295   in the field could help to reduce the non-uniqueness of the inversion. A more dense net of water resistivity measurements would
be helpful and Arboleda-Zapata et al. (2022) suggested that sampling of the sediment to narrow down its electrical resistivity
may help to identify the boundary between frozen and unfrozen ground more precisely. Furthermore, the comparison with
borehole data would be very valuable. Unfortunately, the boreholes available at the northern shore of Tuktoyaktuk are located
in shallow water and were not reachable with the boat on our campaign in 2021. Future surveys may include measurements
300   were the end of the cable is manually pulled towards the shore, so that shallow parts can be covered while the boat stays in
deeper water.

4.3 Permafrost degradation

We observe two distinct permafrost settings north and south of Tuktoyaktuk Island, each of which is explained by a different landscape evolution. North of the island, marine transgression led to an inundation and warming of continuous permafrost, resulting in degradation. The mean annual permafrost degradation rate decreases with increasing distance from the coastline (and thus greater inundation times) due to a weakening of the chemical and thermal gradient with increasing IBPT depth (Angelopoulos et al., 2019; Hutter and Straughan, 1997, 1999). The degradation rates calculated from the IBPT depths over the inundation times of boreholes 2 and 4 are 10.2 cm/yr and 6.6 ± 3.0 cm/yr respectively, thus also indicating faster degradation closer to shore. However, the calculated degradation rate and its uncertainty range must be treated with caution as we are neglecting the error in inundation time induced by varying coastal erosion rates within the past approximately 270 years. South of Tuktoyaktuk Island, the setting is different and the IBPT dips more steeply than on the northern side, to depths of over 20 m bsl at less than 100 m from the coast. At these depths, the sensitivity of the geoelectrical measurements is drastically reduced (Sellmann et al., 1989; Arboleda-Zapata et al., 2022). More advanced degradation is expected as the southern shoreline currently retreats at least four times more slowly than the northern shoreline, which implies longer inundation times at similar distances from the shore. However, a very deep IBPT or even the absence of permafrost within the depth of investigation of the ERT might also be the result of taliks that were present prior to marine submergence. Such taliks would have existed below thermokarst lakes or river channels associated with the former outlet that shaped the Tuktoyaktuk harbor basin. Our bathymetric records locally show water depths exceeding 20 m to the south of Tuktoyaktuk Island, which may be the result of dredging, pre-inundation thermokarst lake floor position, seafloor subsidence following permafrost thaw or some combination.

The comparison between the data presented here from Tuktoyaktuk Island and other data from the Beaufort Sea shows that the IBPT at Tuktoyaktuk is a few meters deeper (for the same inundation time) than at other locations for which comparable data are available (Harding-Lawson-Associates, 1979; Osterkamp et al., 1989; Taylor et al., 1996; Angelopoulos et al., 2020). In the Alaskan Beaufort Sea, e.g., the IBPT is at least twice as deep as on the Canadian shelf, close to the Mackenzie Delta (Harding-Lawson-Associates, 1979). This also applies to inundation times of several thousands of years (Harding-Lawson-Associates, 1979; Osterkamp et al., 1989). As first explained by Harrison and Osterkamp (1978), the coarse sediments of the Canadian Beaufort shelf could facilitate density-driven salt flow to the phase boundary, thereby enhancing salt diffusion at the IBPT and degradation of the IBPT. However, the discharge of the Mackenzie Delta is likely to be the dominant factor influencing the relatively rapid IBPT degradation. The year-round freshwater input leads to particularly warm mean annual bottom temperatures (especially in shallow waters with <10 m depth), accelerating subsea permafrost degradation (Taylor et al., 2013). A similar effect has been observed at Muostakh Island, influenced by the Lena River discharge (Overduin et al., 2016; Shakhova et al., 2017).

5 Conclusions

In our study we present the use of marine electrical resistivity data to determine the depth to the top of the subsea permafrost table at Tuktoyaktuk Island, a natural permafrost-stabilized barrier that protects the harbour of the hamlet of Tuktoyaktuk. We

335 illustrated a possible analysis strategy that accounts for potential inaccuracies arising from the survey design, ambiguities of different inversion types and the difficulty to infer a layer boundary from a resistivity model.

Our findings indicate a slowly dipping permafrost table north of Tuktoyaktuk Island that is concordant with the relatively fast coastal erosion rate there. In contrast, south of the island, where the coastal erosion is significantly slower, the IBPT dips more steeply. Based on the historical coastal retreat rates, we inferred a mean vertical permafrost degradation rate north of the 340 island of $5.3 \pm 4.0\,\mathrm{cm/yr}$.

We highlighted the potential of marine geoelectric surveys as well as the difficulties and possible measures for further improvement in both field work and data analysis in order to narrow down the uncertainty of IBPT depths. Our filtering approach allowed us to rely on soundings with a minimal positional error in the inversion. We addressed the ambiguity of different LCI parametrizations by testing them on a representative synthetic model and presented approaches to simplify data 345 processing and interpretation for future field campaigns. Precise electrode positioning or more frequent CTD measurements e.g., promise to increase the reliability of the inversion and thus to make its interpretation easier.

Data availability. The CTD and ERT data used in this study are available online at https://doi.org/10.1594/PANGAEA.949258 and https://doi.pangaea.de/10.1594/PANGAEA.949499, respectively.

Video supplement. Video of the boat and continuous ERT survey with floating electrode array is available at the Youtube channel Polar 350 Geography: https://www.youtube.com/watch?v=wQdzIK0bL5A&list=PLnngXB12Nji_qQsKX3XiwNO-n1H1P0YVF&index=5

Author contributions. Conceptualization of the work was carried out by EE, MA, PO. Fieldwork, investigations, formal analysis and visualizations were carried out by EE, JB, PPO. Paper writing and editing was led by EE and shared by all authors. Project leadership was provided by JB and PPO.

Competing interests. The contact author has declared that none of the authors has any competing interests.

355 *Acknowledgements.* Critical logistical support for field measurements was provided by Keevik Enterprises Ltd. in Tuktoyaktuk, Canada. We thank Bill Cable, Christian Haberland, Frederieke Miesner and Trond Ryberg for invaluable assistance in the field and for fruitful collaboration within the Helmholtz MOSES project. This work is supported by the Helmholtz Association within the framework of the MOSES (Modular Observation Solutions for Earth Systems) project. This research has been supported by the European Union's Horizon 2020 research and innovation program under grant agreement 773421 (Nunataryuk Project).

References

360 Angelopoulos, M.: Mapping subsea permafrost with electrical resistivity surveys, Nature Reviews Earth & Environment, 3, 6–6, https://doi.org/10.1038/s43017-021-00258-5, 2022.

Angelopoulos, M., Westermann, S., Overduin, P., Faguet, A., Olenchenko, V., Grosse, G., and Grigoriev, M. N.: Heat and salt flow in subsea permafrost modeled with CryoGRID2, J. Geophys. Res.-Earth, 124, 920–937, https://doi.org/10.1029/2018jf004823, 2019.

365 Angelopoulos, M., Overduin, P. P., Miesner, F., Grigoriev, M. N., and Vasiliev, A. A.: Recent advances in the study of Arctic submarine permafrost, Permafrost Periglac., 31, 442–453, https://doi.org/10.1002/ppp.2061, 2020.

Angelopoulos, M., Overduin, P. P., Jenrich, M., Nitze, I., Günther, F., Strauss, J., Westermann, S., Schirrmeister, L., Kholodov, A., Krautblatter, M., et al.: Onshore thermokarst primes subsea permafrost degradation, Geophys. Res. Lett., 48, e2021GL093 881, https://doi.org/10.1029/2021gl093881, 2021.

370 Arboleda-Zapata, M., Angelopoulos, M., Overduin, P. P., Grosse, G., Jones, B. M., and Tronicke, J.: Exploring the capabilities of electrical resistivity tomography to study subsea permafrost, Cryosphere, 16, 4423–4445, https://doi.org/10.5194/tc-16-4423-2022, 2022.

Auken, E., Christiansen, A. V., Jacobsen, B. H., Foged, N., and Sørensen, K. I.: Piecewise 1D laterally constrained inversion of resistivity data, Geophys. Prospect., 53, 497–506, https://doi.org/10.1111/j.1365-2478.2005.00486.x, 2005.

Baird: Tuktoyaktuk Coastal Erosion Study: Data Review, Modelling, Mapping and Erosion Assessment, Tech. rep., W.F. Baird & Associates
375 Coastal Engineers Ltd., 2019a.

Baird: Tuktoyaktuk Coastal Erosion Study: Erosion Mitigation Plan, Tech. rep., W.F. Baird & Associates Coastal Engineers Ltd., 2019b.

Baird: Tuktoyaktuk Shoreline Protection Project, Tech. rep., W.F. Baird & Associates Coastal Engineers Ltd., 2020.

Berry, H. B., Whalen, D., and Lim, M.: Long-term ice-rich permafrost coast sensitivity to air temperatures and storm influence: lessons from Pullen Island, Northwest Territories, Canada, Arctic Science, 7, 723–745, https://doi.org/10.1139/as-2020-0003, 2021.

380 Boike, J. and Dallimore, S. R.: Summary of 2018 Mackenzie Delta permafrost field campaign (mCAN2018), Northwest Territories, Geol. Surv. of Can., Open File Rep 8640, https://doi.org/10.4095/315704, 2019.

Dallimore, S., Fraser, P., Whalen, D., and Magen, C.: Field Report – Tuktoyaktuk Island – Permafrost Drilling Program, Tech. rep., Geol. Surv. of Can., 2018.

Dallimore, S. R., Wolfe, S. A., and Solomon, S. M.: Influence of ground ice and permafrost on coastal evolution, Richards Island, Beaufort
385 Sea coast, N.W.T., Can. J. Earth Sci., 33, 664–675, https://doi.org/10.1139/e96-050, 1996.

Fortier, R., Allard, M., and Seguin, M.-K.: Effect of physical properties of frozen ground on electrical resistivity logging, Cold Reg. Sci. Technol., 22, 361–384, https://doi.org/10.1016/0165-232x(94)90021-3, 1994.

GRID-Arendal: Executive Summary, Rapid Response Assessment of Coastal and Offshore Permafrost, https://storymaps.arcgis.com/stories/9155a51e8aec41838702c8c5ef3382e3, 2020.

390 Hansen, J., Ruedy, R., Sato, M., and Lo, K.: Global surface temperature change, Rev. Geophys., 48, RG4004, https://doi.org/10.1029/2010rg000345, 2010.

Harding-Lawson-Associates: USGS Technical Investigation Beaufort Sea-1979, Tech. rep., U.S. Geol. Surv., 1979.

Harrison, W. and Osterkamp, T. E.: Heat and mass transport processes in subsea permafrost 1. An analysis of molecular diffusion and its consequences, J. Geophys. Res-Oceans, 83, 4707–4712, https://doi.org/10.1029/JC083iC09p04707, 1978.

395 Hu, K., Issler, D., Chen, Z., and Brent, T.: Permafrost investigation by well logs, and seismic velocity and repeated shallow temperature surveys, Beaufort-Mackenzie Basin, Geol. Surv. of Can., Open File Rep. 6956, 228 pp., https://doi.org/10.4095/293120, 2013.

Hutter, K. and Straughan, B.: Penetrative convection in thawing subsea permafrost, Continuum Mech. Therm., 9, 259–272, https://doi.org/10.1007/s001610050070, 1997.

Hutter, K. and Straughan, B.: Models for convection in thawing porous media in support for the subsea permafrost equations, J. Geophys.

400   Res-Sol. Ea., 104, 29 249–29 260, https://doi.org/10.1029/1999JB900288, 1999.

Hynes, S., Solomon, S., and Whalen, D.: GIS compilation of coastline variability spanning 60 years in the Mackenzie Delta and Tuktoyaktuk in the Beaufort Sea, Natural Resources Canada, https://doi.org/10.4095/295579, 2014.

Irrgang, A. M., Lantuit, H., Gordon, R. R., Piskor, A., and Manson, G. K.: Impacts of past and future coastal changes on the Yukon coast—threats for cultural sites, infrastructure, and travel routes, Arctic Science, 5, 107–126, https://doi.org/10.1139/as-2017-0041, 2019.

405   Kitover, D., Van Balen, R., Vandenberghe, J., Roche, D. M., and Renssen, H.: LGM permafrost thickness and extent in the Northern Hemisphere derived from the Earth System Model iLOVECLIM, Permafrost Periglac., 27, 31–42, https://doi.org/10.1002/ppp.1861, 2016.

Kokelj, S. V., Lantz, T. C., Solomon, S., Pisaric, M. F., Keith, D., Morse, P., Thienpont, J. R., Smol, J. P., and Esagok, D.: Using multiple sources of knowledge to investigate northern environmental change: regional ecological impacts of a storm surge in the outer Mackenzie Delta, NWT, Arctic, 65, 257–272, 2012.

410   Lapham, L. L., Dallimore, S. R., Magen, C., Henderson, L. C., Powers, L. C., Gonsior, M., Clark, B., Côté, M., Fraser, P., and Orcutt, B. N.: Microbial greenhouse gas dynamics associated with warming coastal permafrost, Western Canadian Arctic, Front. Earth Sci., 8, 582 103, https://doi.org/10.3389/feart.2020.582103, 2020.

Lenssen, N. J., Schmidt, G. A., Hansen, J. E., Menne, M. J., Persin, A., Ruedy, R., and Zyss, D.: Improvements in the GISTEMP uncertainty model, J. Geophys. Res-Atmos, 124, 6307–6326, https://doi.org/https://doi.org/10.1029/2018JD029522, 2019.

415   Loke, M.: Tutorial: 2-D and 3-D Electrical Imaging Surveys, https://www.researchgate.net/publication/264739285_Tutorial_2-D_and_3-D_Electrical_Imaging_Surveys, 2001.

Manson, G. K. and Solomon, S. M.: Past and future forcing of Beaufort Sea coastal change, Atmos. Ocean, 45, 107–122, https://doi.org/10.3137/ao.450204, 2007.

Miesner, F., Overduin, P., Grosse, G., Strauss, J., Langer, M., Westermann, S., Schneider von Deimling, T., Brovkin, V., and Arndt, S.: Subsea

420   permafrost organic carbon stocks are large and of dominantly low reactivity, Sci. Rep.-UK, 13, 9425, https://doi.org/10.1038/s41598-023-36471-z, 2023.

Osterkamp, T., Baker, G., Harrison, W., and Matava, T.: Characteristics of the active layer and shallow subsea permafrost, J. Geophys. Res-Oceans, 94, 16 227–16 236, https://doi.org/10.1029/JC094iC11p16227, 1989.

Overduin, P., Schneider von Deimling, T., Miesner, F., Grigoriev, M., Ruppel, C., Vasiliev, A., Lantuit, H., Juhls, B., and Westermann, S.:

425   Submarine permafrost map in the Arctic modeled using 1-D transient heat flux (supermap), J. Geophys. Res-Oceans, 124, 3490–3507, https://doi.org/10.1029/2018jc014675, 2019.

Overduin, P. P., Westermann, S., Yoshikawa, K., Haberlau, T., Romanovsky, V., and Wetterich, S.: Geoelectric observations of the degradation of nearshore submarine permafrost at Barrow (Alaskan Beaufort Sea), J. Geophys. Res.-Earth, 117, https://doi.org/10.1029/2011jf002088, 2012.

430   Overduin, P. P., Wetterich, S., Günther, F., Grigoriev, M. N., Grosse, G., Schirrmeister, L., Hubberten, H.-W., and Makarov, A.: Coastal dynamics and submarine permafrost in shallow water of the central Laptev Sea, East Siberia, Cryosphere, 10, 1449–1462, https://doi.org/10.5194/tc-10-1449-2016, 2016.

Ramage, J., Jungsberg, L., Wang, S., Westermann, S., Lantuit, H., and Heleniak, T.: Population living on permafrost in the Arctic, Popul. Environ., 43, 22–38, https://doi.org/10.1007/s11111-020-00370-6, 2021.

435   Rantanen, M., Karpechko, A. Y., Lipponen, A., Nordling, K., Hyvärinen, O., Ruosteenoja, K., Vihma, T., and Laaksonen, A.: The Arctic has warmed nearly four times faster than the globe since 1979, Communications Earth & Environment, 3, 1–10, https://doi.org/10.1038/s43247-022-00498-3, 2022.

Rücker, C., Günther, T., and Wagner, F. M.: pyGIMLi: An open-source library for modelling and inversion in geophysics, Computers and Geosciences, 109, 106–123, https://doi.org/10.1016/j.cageo.2017.07.011, 2017.

440   Schuur, E. A., McGuire, A. D., Schädel, C., Grosse, G., Harden, J. W., Hayes, D. J., Hugelius, G., Koven, C. D., Kuhry, P., Lawrence, D. M., et al.: Climate change and the permafrost carbon feedback, Nature, 520, 171–179, https://doi.org/10.1038/nature14338, 2015.

Sellmann, P. V., Delaney, A. J., Arcone, S. A., et al.: Coastal subsea permafrost and bedrock observations using dc resisitivity, Tech. rep., Cold Regions Research and Engineering Laboratory (US), 1989.

Shakhova, N., Semiletov, I., Gustafsson, O., Sergienko, V., Lobkovsky, L., Dudarev, O., Tumskoy, V., Grigoriev, M., Mazurov, A., Salyuk,
445   A., et al.: Current rates and mechanisms of subsea permafrost degradation in the East Siberian Arctic Shelf, Nat. Commun., 8, 15 872, https://doi.org/10.1038/ncomms15872, 2017.

Solomon, S. M.: Spatial and temporal variability of shoreline change in the Beaufort-Mackenzie region, Northwest Territories, Canada, Geo-Mar. Lett., 25, 127–137, https://doi.org/10.1007/s00367-004-0194-x, 2005.

Solomon, S. M., Taylor, A. E., and Stevens, C. W.: Nearshore ground temperatures, seasonal ice bonding, and permafrost formation within
450   the bottom-fast ice zone, Mackenzie Delta, NWT, in: Proceedings of the Ninth International Conference on Permafrost, Fairbanks, Alaska, vol. 29, pp. 1675–1680, Institute of Northern Engineering, University of Alaska Fairbanks Fairbanks, 2008.

Taylor, A. E., Dallimore, S. R., and Outcalt, S.: Late Quaternary history of the Mackenzie–Beaufort region, Arctic Canada, from modelling of permafrost temperatures. 1. The onshore–offshore transition, Can. J. Earth Sci., 33, 52–61, https://doi.org/10.1139/e96-006, 1996.

Taylor, A. E., Dallimore, S., Hill, P., Issler, D., Blasco, S., and Wright, F.: Numerical model of the geothermal regime on the Beaufort Shelf,
455   arctic Canada since the Last Interglacial, J. Geophys. Res.-Earth, 118, 2365–2379, https://doi.org/10.1002/2013JF002859, 2013.

Whalen, D., Forbes, D. L., Kostylev, V., Lim, M., Fraser, P., Nedimović, M. R., and Stuckey, S.: Mechanisms, volumetric assessment, and prognosis for rapid coastal erosion of Tuktoyaktuk Island, an important natural barrier for the harbour and community, Can. J. Earth Sci., https://doi.org/10.1139/cjes-2021-0101, 2022.

Wilkenskjeld, S., Miesner, F., Overduin, P. P., Puglini, M., and Brovkin, V.: Strong increase in thawing of subsea permafrost in the 22nd
460   century caused by anthropogenic climate change, Cryosphere, 16, 1057–1069, https://doi.org/10.5194/tc-16-1057-2022, 2022.